Strong-motion Broadband Displacements from Collocated Ocean-bottom Pressure Gauges and Seismometers

Ayumu Mizutani[1, 2], Diego Melgar[2], and Kiyoshi Yomogida[1]

[1]Department of Earth and Planetary Sciences, Faculty of Sciences, Hokkaido University, Sapporo, Japan.

[2]Department of Earth Sciences, University of Oregon, Eugene, Oregon, U.S.A.

Corresponding author: A. Mizutani (mizutaniayumumail@gmail.com)

Key Points:

- Propose a new method to estimate the near-fault displacement waveform associated with an offshore earthquake.
- The method utilizes the collocated strong-motion seismometer and ocean-bottom pressure gauge.
- The obtained displacement waveforms improved the finite fault model.

Abstract

Dense and broad-coverage ocean-bottom observation networks enable us to obtain near-fault displacement records associated with an offshore earthquake. However, simple integration of ocean-bottom strong-motion acceleration records leads to physically unrealistic displacement records. Here we propose a new method using a Kalman filter to estimate coseismic displacement waveforms using the collocated ocean-bottom seismometers and pressure gauges. First, we evaluate our method using synthetic records and then apply it to an offshore Mw 6.0 event that generated a small tsunami. In both the synthetic and real cases, our method successfully estimates reasonable displacement waveforms. Additionally, we show that the computed waveforms improve the results of the finite fault modeling process. In other words, the proposed method will be useful for estimating the details of the rupture mechanism of offshore earthquakes as a complement to onshore observations.

Plain language summary

Ocean-bottom observations enable us to obtain near-fault displacement records associated with an offshore earthquake. However, simple integration of ocean-bottom acceleration records leads to physically unrealistic displacement records. Here we propose a new method to estimate offshore coseismic displacement waveforms. First, we evaluate our method using synthetic records and then apply it to an offshore earthquake that generated a small tsunami. In both cases, our method successfully estimates reasonable displacements. Additionally, we show that the computed waveforms improve the results of the earthquake source modeling process. In other words, the proposed method will be useful for estimating the details of the rupture mechanism of offshore earthquakes as a complement to onshore observations.

1 Introduction

Recently, real-time ocean-bottom seismometer networks have been deployed at active tectonic margins for the dual purpose of both basic research and real-time monitoring (e.g., S-net and DONET in Japan, NEPTUNE in Canada, and OOI in the US; Aoi et al., 2020; Barnes & Team, 2007; Trowbridge et al., 2019). These networks enable us to obtain near-fault records associated with an offshore earthquake. When coseismic deformation is large enough, tsunamis occur due to such events and can damage coastal areas. Coseismic displacement records at near-fault stations are thus important because they have the potential to help in evaluating the earthquake source and its resulting tsunami quickly – this can improve the performance of early warning systems. In addition, they can be useful in estimating the details of the rupture mechanism of offshore earthquakes as a complement to onshore observations.

The ocean-bottom record has complicated noise sources for seismic recordings of any kind (e.g., Hilmo & Wilcock, 2020; Webb, 1998), more so than in the onshore environment. Ideally, we seek to obtain a displacement waveform through the double integrations of an acceleration or "strong motion" record. However, even in the simpler situation of onshore recordings, simple integration leads to unphysical results due to "baseline offsets" which are small shifts in the records (Iwan et al., 1985). Many schemes have been proposed to remove the drifts in onshore strong-motion records (e.g., Boore, 2001; Wu & Wu, 2007; Wang et al., 2011). These can often succeed in baseline correction, but their convergence is not always guaranteed, and even more worrying, even if they do converge it is not always the case that they converge to the right final static offset (Boore et al., 2002). Additionally, baseline correction is difficult to apply in real-time settings. Alternatively, Bock et al. (2011) applied a Kalman filter approach to the records of the collocated high-rate Global Navigation Satellite System (HR-GNSS) and seismometer sites, and succeeded in estimating the displacement waveform. Lately, many papers expanded on the use of the Kalman filter approach with onshore records (e.g., Geng et al., 2013; Melgar et al., 2013; Niu & Xu, 2014; Tu et al., 2014; Zang et al., 2019).

In this study, we propose a new method to estimate the coseismic displacement waveforms from offshore strong-motion records. We base the approach on the general philosophy of Bock et al. (2011): using the Kalman filter and combining the strong-motion record with the collocated ocean-bottom pressure gauge (OBPG) records. However, we have added challenges in the offshore environment, since a coseismic OBPG record contains not only seafloor displacements but also seafloor accelerations, ocean acoustic waves, and tsunamis (Saito, 2013), we cannot use the same Kalman filter formulation employed for onshore records. Section 2 explains the innovation of the Kalman filter approach proposed in this study. Then we apply it to synthetic data (Section 3) and real data for an M_w 6.0 earthquake recorded offshore in the Nankai, Japan region (Section 4). Finally, in Section 5, the estimated displacement waveforms are evaluated through the finite fault modeling.

Note that our method focuses only on vertical displacement because OBPGs are only sensitive to physical phenomena that can be leveraged to calculate vertical displacement. Unless otherwise described all the variables in the later sections are the vertical component.

2 Kalman filter implementation

The Kalman filter is an optimal estimation method based on the state-space representation of a dynamic system (Kalman, 1960). It consists of the combination of two different models: (1) the dynamic model which captures the physics of the processes involved and describes the time evolution of the states, and (2) the observation model which establishes the relationship between measurements and the states. The models used in this study are expressed as:

$$\frac{d}{dt}\begin{bmatrix} d \\ v \\ \Omega \\ \eta \end{bmatrix} = \begin{bmatrix} 0 & 1 & 0 & 0 \\ 0 & 0 & -1 & 0 \\ 0 & 0 & 0 & 0 \\ 0 & 1 & 0 & 0 \end{bmatrix}\begin{bmatrix} d \\ v \\ \Omega \\ \eta \end{bmatrix} + \begin{bmatrix} 0 & 0 \\ 1 & 0 \\ 0 & 0 \\ 0 & 1 \end{bmatrix}\begin{bmatrix} a \\ \dot{h} \end{bmatrix} + \begin{bmatrix} 0 \\ \varepsilon^{a} \\ \varepsilon^{\Omega} \\ \varepsilon^{\dot{h}} \end{bmatrix}, \#(1)$$

$$\begin{bmatrix} h \\ \tilde{\eta} \end{bmatrix} = \begin{bmatrix} -1 & 0 & 0 & 1 \\ 0 & 0 & 0 & 1 \end{bmatrix}\begin{bmatrix} d \\ v \\ \Omega \\ \eta \end{bmatrix} + \begin{bmatrix} \varepsilon^{h} \\ \varepsilon^{\tilde{\eta}} \end{bmatrix}, \#(2)$$

where d, v, η, and Ω are the displacement, velocity, tsunami height, and DC offset of acceleration. The variables of ε are the properties of noise in estimation. The DC offset is defined by the difference in baselines between the observed acceleration a^{obs} and the true acceleration a^{true}: $\Omega = a^{obs} + \varepsilon^{a} - a^{true}$ (Melgar et al., 2013). The vector $[\,d \quad v \quad \Omega \quad \eta]^{T}$ is thus the state vector, the output or result of the Kalman filter estimator. In this study, we use the water-depth fluctuation $h = \eta - d$ and estimated tsunami height $\tilde{\eta}$ as the observation (Eq. 2). Note that $\dot{h}$ in Eq. 1 is the time derivative of h; h and $\tilde{\eta}$ are independently estimated by any methods other than the Kalman filter as we'll discuss soon. The noise properties of each variable, ε, are considered to be the Gaussian with zero mean and a standard deviation, i.e., $\varepsilon \sim N(0, \sigma)$, and independent of each other.

Because Eqs. 1 and 2 are for continuous time series, an extra step in the derivation is needed to discretize them (Lewis et al., 2008):

$$\begin{bmatrix} d_{t+1} \\ v_{t+1} \\ \Omega_{t+1} \\ \eta_{t+1} \end{bmatrix} = \begin{bmatrix} 1 & \Delta t & -\frac{\Delta t^2}{2} & 0 \\ 0 & 1 & -\Delta t & 0 \\ 0 & 0 & 1 & 0 \\ 0 & \Delta t & -\frac{\Delta t^2}{2} & 1 \end{bmatrix} \begin{bmatrix} d_t \\ v_t \\ \Omega_t \\ \eta_t \end{bmatrix} + \begin{bmatrix} \frac{\Delta t^2}{2} & 0 \\ \Delta t & 0 \\ 0 & 0 \\ \frac{\Delta t^2}{2} & \Delta t \end{bmatrix} \begin{bmatrix} a_t \\ \dot{h}_t \end{bmatrix} + q_t, \#(3)$$

$$\begin{bmatrix} h_t \\ \tilde{\eta}_t \end{bmatrix} = \begin{bmatrix} -1 & 0 & 0 & 1 \\ 0 & 0 & 0 & 1 \end{bmatrix} \begin{bmatrix} d_t \\ v_t \\ \Omega_t \\ \eta_t \end{bmatrix} + r_t, \#(4)$$

where Δt is the time interval of the dynamic model (0.01 sec in our case, which is the sample rate of the ocean bottom accelerometer); q_t and r_t are the Gaussian noise such as $q_t \sim N(0, \boldsymbol{Q}_t)$ and $r_t \sim N(0, \boldsymbol{R}_t)$, respectively. The covariance matrices, $\boldsymbol{Q}_t$ and $\boldsymbol{R}_t$, are written as:

$$\boldsymbol{Q}_t = \begin{bmatrix} 0 & \sigma_t^a \Delta t^2/2 & 0 & 0 \\ \sigma_t^a \Delta t^2/2 & \sigma_t^a \Delta t & -\sigma_t^\Omega \Delta t^2/2 & \sigma_t^a \Delta t^2/2 \\ 0 & -\sigma_t^\Omega \Delta t^2/2 & \sigma_t^\Omega \Delta t & 0 \\ 0 & \sigma_t^a \Delta t^2/2 & 0 & \sigma_t^{\dot{h}} \Delta t \end{bmatrix}, \#(5)$$

$$\boldsymbol{R}_t = \begin{bmatrix} \sigma_t^h/\Delta\tau & 0 \\ 0 & \sigma_t^{\tilde{\eta}}/\Delta\tau \end{bmatrix}, \#(6)$$

where $\Delta\tau$ is the time interval of the observation model (1 sec in our case, which is the sample rate of h and $\tilde{\eta}$). If Δt and $\Delta\tau$ are equal, Eqs. 3 and 4 are applied at every time step. If not, Eq. 4 is only applied when a measurement, $[h_t \quad \tilde{\eta}_t]^T$, is available or every $\Delta\tau$. Note that as in Bock et al. (2011), we apply not only the Kalman filter but also the Kalman smoother which is applied backwards in time.

Before applying the Kalman filter, we need to obtain h and $\tilde{\eta}$ independently of the ongoing estimation. In this study, they are estimated by the method proposed by Mizutani et al. (2020), extracting the tsunami and displacement components from the coseismic OBPG records on a real-time basis, and the tsunami source model estimated by the tsunami waveform inversion using time-derivative waveform (Kubota et al., 2018), respectively (Fig. 1). When calculating $\tilde{\eta}$, we assume that the tsunami occurs instantaneously, or, put another way that the rise time for the deformation of the seafloor and sea surface can be negligible. The tsunami inversion is regularized using spatial smoothing. The weight factor, or the strength of regularization, is determined based on the trade-off curve between the variance reduction (VR) and the model variance. The details of the inversion methods and the trade-off curves are given in Text S1 and Fig. S1.

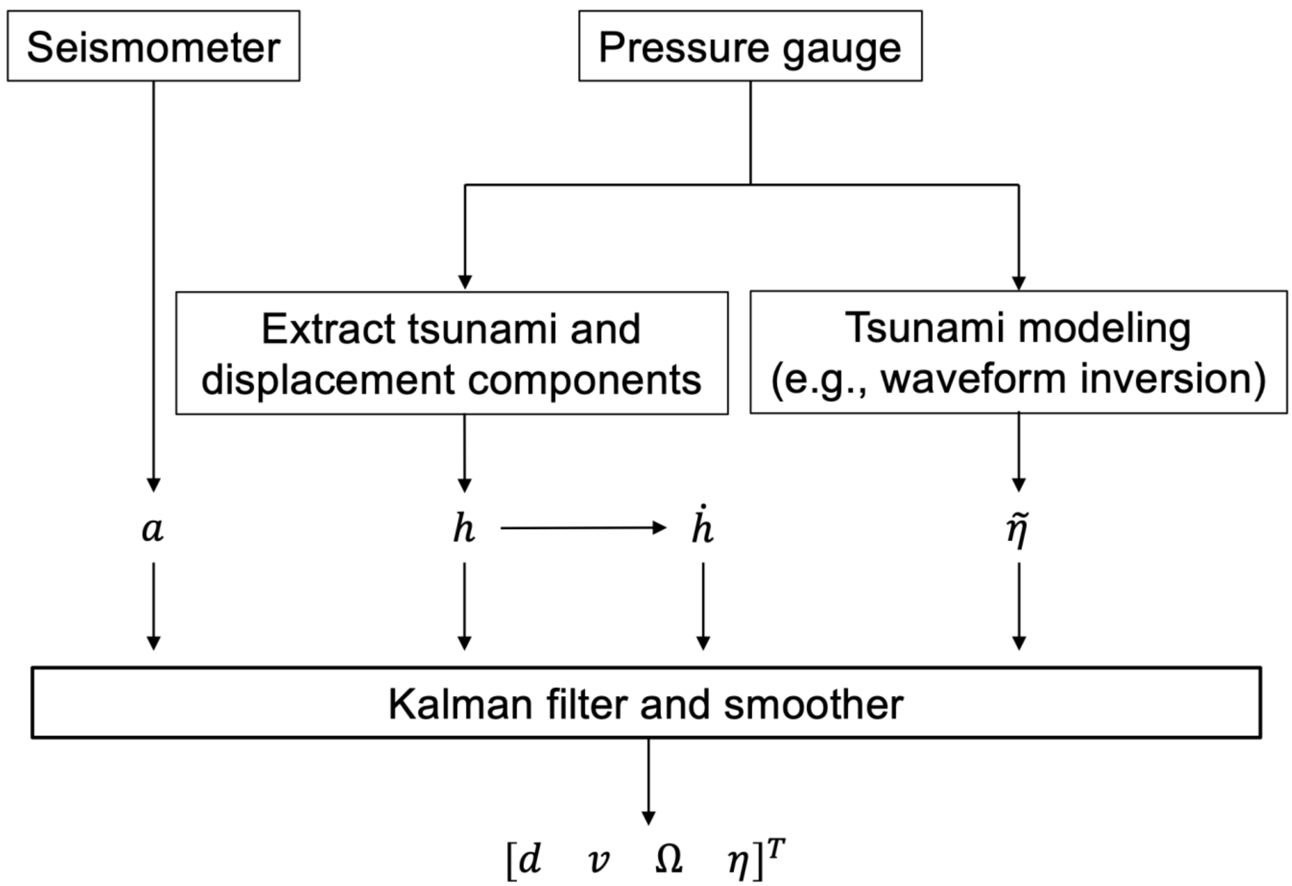

Figure 1. *The schematic flow of the proposed method.*

The covariance matrices, $\boldsymbol{Q}_t$ and $\boldsymbol{R}_t$, or the variances of each variable, σ_t, are important tuning parameters of the Kalman filter. We propose them to be automatically calculated from the records by moving time windows. For the strong-motion records, σ_t^a is the moving variance of a and σ_t^Ω is the absolute value of the moving average of a; the 5-sec window is used in both cases. Since h_t is estimated as the difference between two filtered records with a moving taper window (Mizutani et al., 2020, Section 5.1), σ_t^h is the sum of the variance of filtered records with the range of the taper's flat part (48 sec). Using σ_t^h, $\sigma_t^{\dot{h}}$ is calculated as $(\sigma_t^h + \sigma_{t-1}^h)/\Delta t$. Finally, $\sigma_t^{\tilde{\eta}}$ is defined as the diagonal elements of $\boldsymbol{G}_{\mathrm{forward}}\boldsymbol{G}_{\mathrm{inv}}^{-1}[\mathrm{cov}\,\boldsymbol{p}][\boldsymbol{G}_{\mathrm{forward}}\boldsymbol{G}_{\mathrm{inv}}^{-1}]^T$, where $\boldsymbol{G}_{\mathrm{inv}}$ and $\boldsymbol{G}_{\mathrm{forward}}$ are the kernel matrices used in the waveform inversion and forward calculation; $[\mathrm{cov}\,\boldsymbol{p}]$ is the covariance matrix of the data used in the inversion, that is, the diagonal matrix whose elements are $(\sigma_t^p + \sigma_{t-1}^p)/\Delta\tau$, where σ_t^p is the moving variance of the data with a time window of 60 sec. Note that we do not use σ_t^p but $(\sigma_t^p + \sigma_{t-1}^p)/\Delta\tau$ because the waveform inversion of Kubota et al. (2018) uses time-derivative waveforms.

3 Synthetic test

In this section, we confirm the validity of our method and assumptions with synthetic records. Based on the methodology of Saito & Tsushima (2016), the records were obtained using opensource software for simulating seismic wave propagation, OpenSWPC (Maeda et al., 2017), and tsunami propagation, GeoClaw (Clawpack Development Team, 2022; Mandli et al., 2016). First, the seafloor acceleration, velocity, displacement, and stress change were calculated by OpenSWPC, and then, GeoClaw calculated the tsunami caused by the seafloor movement under the non-linear long-wave approximation.

A two-layer velocity model was used for the synthetic test: a water layer with P wave speed of 1.5 km and density of 1.0 kg/m^3; a homogeneous sea-bottom layer with P and S wave speed of 7 and 4 km/s and density of 2.7 kg/m^3. The thickness of each layer was 4 and 400 km, and the horizontal dimensions of the model domain were 200 × 200 km. The domain was divided into 0.5 and 1 km cells in the horizontal and vertical direction, respectively, and the time interval was 0.02 sec. The source was represented as a point source whose parameters were as follows: the moment magnitude was 7.0; the strike, dip, and rake were 0°, 45°, and 90° (a pure reverse fault); the depth was 10 km; and the rise time was 7.5 sec. We set this source at the center of the model domain (Fig. 2a).

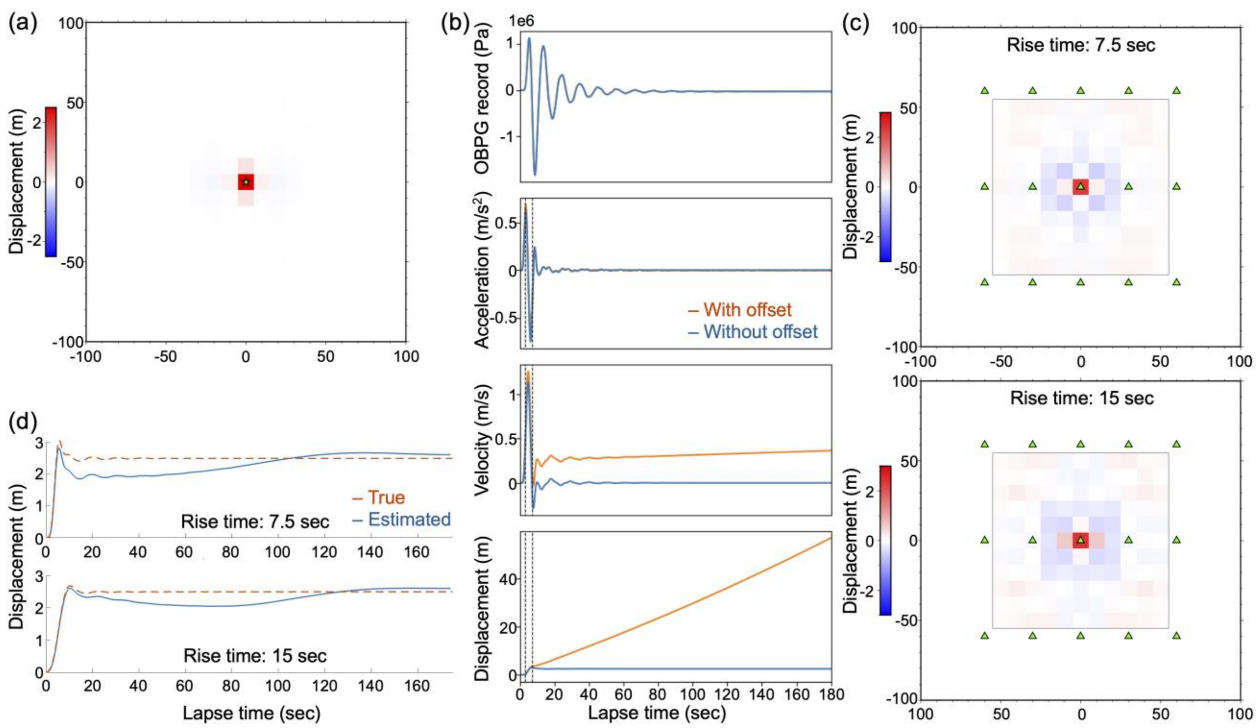

Figure 2. *(a) Sea-bottom residual displacement in the synthetic test. The Green star represents the source location. (b) Synthetic records of ocean-bottom pressure, acceleration, velocity, and displacement at the station directly above the source. The blue lines are the records without noise. The orange line in the acceleration is with the baseline shift, and the lines in the*

displacement and velocity are integrated from it. The black dashed line represents the strong motion duration causing the baseline shift. (c) The result of tsunami waveform inversion for $\tilde{\eta}$ with the rise time of 7.5 sec (top) and 15 sec (bottom). The green triangles and black rectangle represent the stations and target region. (d) Estimated result of the Kalman filter (blue) and true waveform (orange) with the rise time of 7.5 sec (top) and 15 sec (bottom).

Fig. 2b shows the synthetic records directly above the source. The OBPG record had a large amplitude due to the ocean acoustic waves and sea-bottom acceleration. In acceleration records, we added the baseline offset based on the model of Iwan et al. (1985), i.e., strong ground motion causes an offset, and after that, a minor offset still remains. We defined the strong motion for the baseline shift as over 0.5 m/s^2, following Iwan et al. (1985). The offsets during and after the strong motion were 0.07 and 0.0007 m/s^2, which were visually adjusted. Although the baseline shifts slightly affected the acceleration record, they significantly altered the velocity and displacement records. Note that we applied the Kalman filter to the record at this station; others were used only for the tsunami inversion.

The estimated tsunami source model for $\tilde{\eta}$ and the outcoming results of the Kalman filter are shown in Figs. 2c and 2d, respectively. Although the input acceleration was contaminated by the noise, the displacement waveform estimated by our method agreed with the “true” one.

When calculating $\tilde{\eta}$, our method assumes that a tsunami occurs instantaneously. To investigate the effect of the rise time, we conducted the same synthetic test with twice the rise time (15 sec). In this case, the threshold for the baseline shifts in the acceleration was defined as 0.1 m/s^2. The resultant waveforms also agreed with the true one, particularly in the dynamic part of the displacement waveform (Fig. 2d). Since the seafloor and sea surface move simultaneously, it is difficult for the OBPG to observe any dynamic displacement components, that is, this agreement comes from the acceleration record. In other words, the method proposed in this study successfully combined the information of the collocated OBPG and strong-motion seismometer.

4 Application to real data

We used the records of Dense Oceanfloor Network system for Earthquakes and Tsunamis (DONET; Aoi et al., 2020), which is deployed off the coast of Kii Peninsula, Japan (Fig 3a). Each station of this network consists of an ocean-bottom seismometer and an OBPG. On 1 April 2016, an Mw 6.0 event occurred inside this network (e.g., Araki et al., 2017; Takemura et al., 2018). The OBPGs clearly observed the pressure change originated from the tsunami, and strong-motion accelerometer records observed significant shaking (the peak ground acceleration (PGA) was over 0.5 m/s^2 at near-fault stations) and contained clear baseline shifts (Kubota et al., 2018; Mizutani et al., 2020; Wallace et al., 2016). For the preprocessing of the acceleration data, we removed the pre-earthquake offset in the records by taking the mean of the record 10 sec before the earthquake. For the OBPG data, the ocean tide component and the offset were removed by the theoretical tide model (Matsumoto et al., 2000) and the mean of the 30 min of the pre-event record.

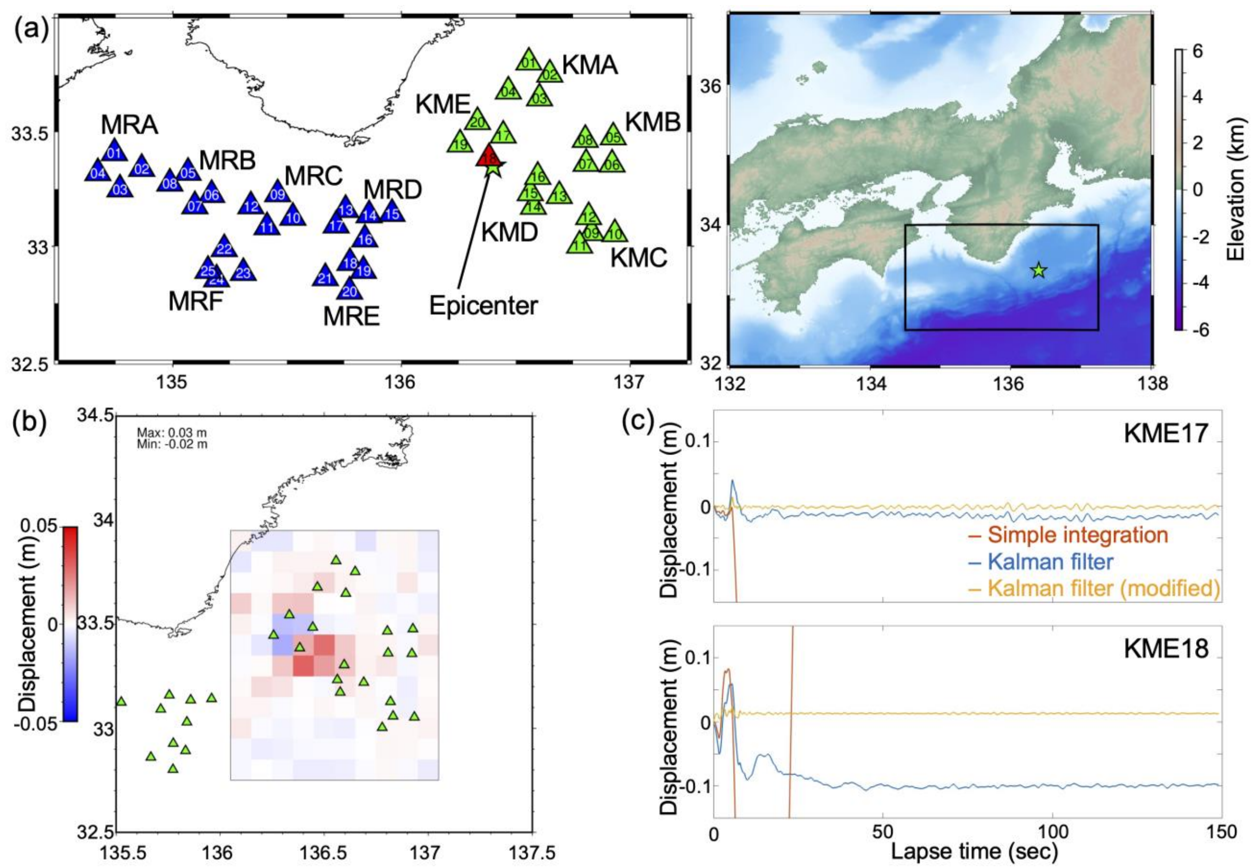

Figure 3. *(a) DONET stations used in this study. The blue, red, and green triangles are the stations used only for the tsunami source inversion, only for the Kalman filter, and for both, respectively. Sets of three characters represent the subarrays of DONET. The green star is the epicenter estimated by Wallace et al. (2016). The black rectangle in the right panel represents the area of the left panel. (b) Tsunami source model for $\tilde{\eta}$ estimated by the tsunami waveform inversion. (c) Displacement waveforms at stations KME17 and KME18 estimated with h of Mizutani et al. (2020) (blue) and with h by the tsunami source inversion (yellow). The Orange lines are the displacements simply integrated from the acceleration record.*

When conducting the tsunami source inversion for $\tilde{\eta}$, we calculated Green's functions with the GEBCO_2023 bathymetry (GEBCO, 2023) with grid intervals of 0.02° from unit sources which were set each 0.1°. Note that we excluded station KME18, the closest station to the source, from the tsunami source inversion as well as Kubota et al. (2018), although applied the Kalman filter to its record. The resultant model is shown in Fig. 3b.

Fig.3c shows the displacement waveforms at stations KME18 and KME17, the second closest station to the source (the results of other stations are shown in Fig. S2). As with the synthetic test (Section 3), we succeeded in obtaining stable displacement waveforms. We, however, must pay attention to the residual displacement or DC component of the waveforms. For example, the waveform at KME18 indicated a subsidence of about 10 cm. The same signal was observed in the OBPG record, which previous studies considered as a false signal (Kubota et al., 2018; Wallace et al., 2016). Since our method estimates the displacement via h from OBPG records (Eq. 4), the residual displacement was affected by such an unphysical offset in OBPG records.

To avoid this problem, we changed a method to estimate h in Eq. 4. We now estimate h from the same model for $\tilde{\eta}$, and the variance σ_t^h was also calculated in the same scheme as $\tilde{\eta}$. Note that this alternative method was applied only to the stations whose OBPG records might have been contaminated by unphysical offsets: KMA03, KME17, and KME18, as suggested by Kubota et al. (2018). The displacement waveforms obtained from this method were also stable (yellow lines in Fig 3c) and the unphysical offsets could be removed. The residual displacements agreed with the one by the tsunami source inversion.

5 Finite fault estimation

To evaluate the utility of the displacement waveforms from Section 4, we next conducted a finite fault inversion and compared the resultant model with the one obtained from the inversion of tsunami records. We solved this linear inverse problem by the non-negative least square method

(Lawson & Hanson, 1995) with spatial smoothing (Text S1 and Fig. S1). Green's functions were calculated by OpenSWPC and GeoClaw. In the seismic waveform calculation, we used the 3-D velocity structure model by Koketsu et al. (2012) with grid intervals of 0.25 km and a time step of 0.01 sec. In the tsunami case, we used the same model in Section 4, i.e., GEBCO_2023 bathymetry with 0.02º interval.

The number of subfaults used was 81, each with a subfault size of 5 × 5 km and a rise time of 3 sec. Here, we estimated only the slip amount at each subfault; the other fault parameters were fixed as the values of Wallace et al. (2016): the strike, dip, and rake were 215°, 5°, and 95°; the center of the fault model was at 33.385ºN and 136.434ºE, and at 9.8 km below the seafloor. We set the rupture speed to 2.1 km/s, 80 % of the S wave speed in this region (Kamei et al., 2012; Wallace et al., 2016).

Fig. 4a shows the result of the inversion using the displacement waveforms. To investigate estimation errors, we conducted a bootstrap method with 200 samples where we randomly selected stations at each iteration (Chernick, 2007). The M_w calculated from this model was 5.9 and the VR was 68.7%. From the standard deviation of the bootstrap (right panel in Fig. 4a), a large slip patch beside the epicenter reflects the actual fault slip, while small one close to station KME20 is perhaps an estimation error. This result is consistent with the aftershock distribution detected by Japan Meteorological Agency (JMA) and the result from the tsunami-only inversion (the Mw and VR were 5.9 and 59%; Fig. 4b). We therefore conclude that the displacement waveforms estimated in Section 4 can be used reliably for studying offshore sources.

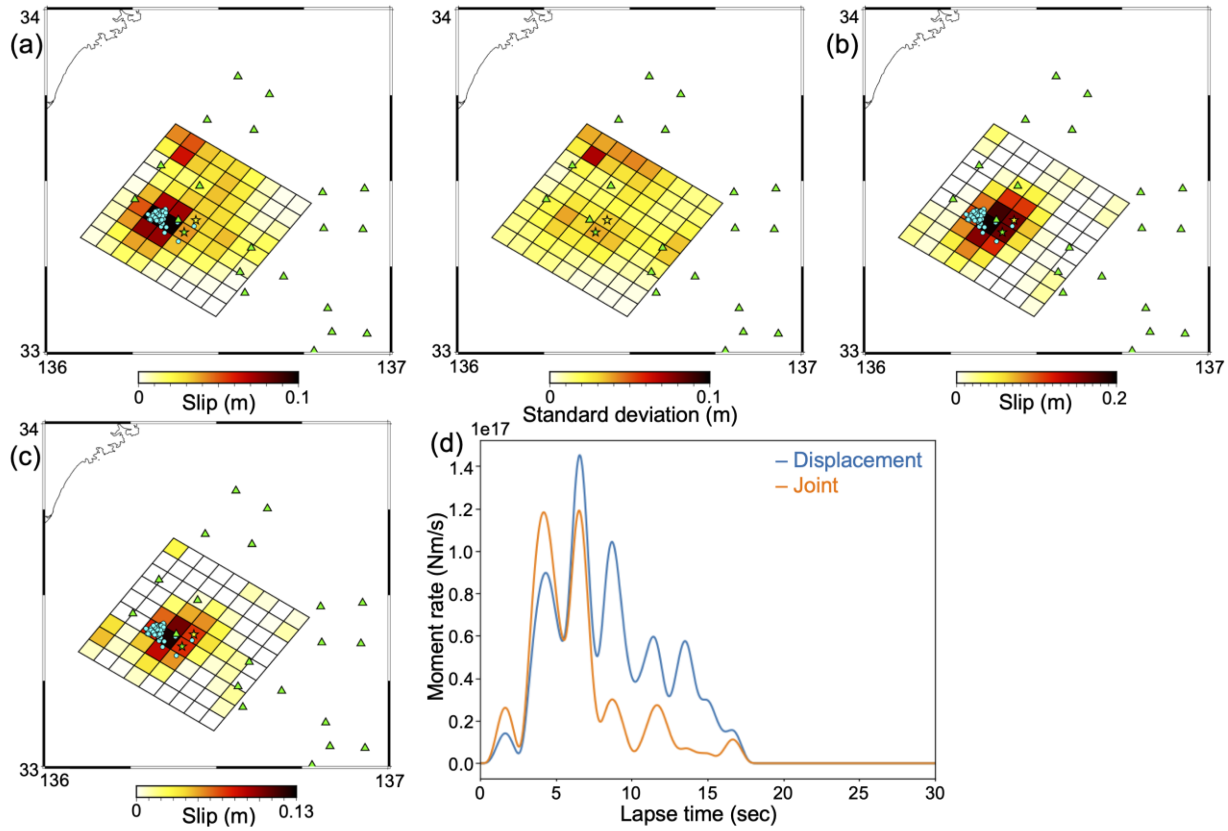

Figure 4. *(a) Slips of the finite fault model (left) and their standard deviations (right) by the bootstrap method with displacement waveforms. The green triangles and blue circles represent DONET stations and aftershocks larger than magnitude 1 detected by JMA, which occurred within two days after the main shock. The green and yellow stars are the epicenter and the fault location estimated by Wallace et al. (2016). (b)(c) Same as (a) except that by the tsunami waveform inversion and by the joint inversion with the displacement and tsunami waveforms. (d) The blue and orange lines represent the source time functions calculated by the models of (a) and (c).*

6 Discussion

To combine displacement and tsunami data, we conducted an additional joint inversion (Text S1 and Fig. S1). The obtained fault model is shown in Fig. 4c. The VR were 57.1% and 44.1% for the displacement and tsunami; the estimated moment magnitude was 5.8. The model indicated that the slip propagated from the epicenter to the downdip direction. Compared to the model from the displacement waveforms only, the fault slip concentrated only around the epicenter. Its extent was also narrower than the model only using the tsunami.

Using the seismic records enables us to calculate the source time function (Fig. 4d). It indicated that a large rupture occurred at 3 sec after the origin time, and lasted 5 sec. The shorter duration compared to the one by the model using the displacement only reflects the slip distribution smaller than that.

Wallace et al. (2016) suggested that the aftershocks associated with this event occurred due to the afterslip immediately following the main shock because their fault model was separated from the aftershock cluster. Our model, on the other hand, agrees with the aftershock distribution and indicates that the aftershocks were caused directly by the main shock, that is, the afterslip may not be necessary for the aftershocks.

The aftershock distribution in Fig. 4 concentrates on the west of the slip. This is because JMA detected the earthquake location using only onshore stations. Araki et al. (2017) found slow-slip events after this earthquake located in the area between stations KME17 and KME18, different from the afterslip proposed by Wallace et al. (2016), which cover the north region of our fault model (Araki et al., 2017, Fig. 2b). In other words, our fault model can explain the aftershock distribution associated with this event sequence very well.

7 Conclusion

We proposed a new method to estimate the coseismic displacement waveform from collocated ocean-bottom strong-motion accelerometers and OBPGs. Through the synthetic test and the application to real data, we confirmed the displacement waveforms estimated by this method to be reliable.

On the other hand, at some stations close to the epicenter, the resultant waveform had a relatively large offset due to unphysical DC components in OBPG records. At present, we cannot remove such an offset automatically because it is difficult to model this offset, that is, cannot be included simply in the Kalman filter estimation. Although several studies investigated unphysical drifts in OBPG records, they focused on the static records (Chadwick et al., 2006; Hino et al., 2022). Clarifying the characteristics of coseismic OBPG records will improve the Kalman filter approach to ocean-bottom records.

The finite fault model that jointly inverted from both the displacement and tsunami waveforms showed improvements compared to the models estimated independently. In other words, the displacement waveform by our method can help us to reveal the details of the rupture process of offshore earthquakes.

Acknowledgments

The records of DONET used in this study were provided by the NIED. This work benefitted from access to the University of Oregon high performance computing cluster, Talapas. This work was partially supported by JSPS KAKENHI grant number 22J10212.

Open Research

DONET records (NIED, 2019) can be downloaded from the NIED website (https://www.hinet.bosai.go.jp/?LANG=en, for strong-motion records; https://www.seafloor.bosai.go.jp, for pressure records) with data request and permission. The codes of OpenSWPC and GeoClaw are freely available from GitHub (https://tktmyd.github.io/OpenSWPC/ and https://github.com/clawpack).

References

Aoi, S., Asano, Y., Kunugi, T., Kimura, T., Uehira, K., Takahashi, N., Ueda, H., Shiomi, K., Matsumoto, T., & Fujiwara, H. (2020). MOWLAS: NIED observation network for earthquake, tsunami and volcano. *Earth, Planets and Space*, *72*(1), 126. https://doi.org/10.1186/s40623-020-01250-x

Araki, E., Saffer, D. M., Kopf, A. J., Wallace, L. M., Kimura, T., Machida, Y., Ide, S., Davis, E., & IODP EXPEDITION 365 SHIPBOARD SCIENTISTS. (2017). Recurring and triggered slow-slip events near the trench at the Nankai Trough subduction megathrust. *Science*, *356*(6343), 1157–1160. https://doi.org/10.1126/science.aan3120

Barnes, C. R., & Team, N. C. (2007). Building the World's First Regional Cabled Ocean Observatory (NEPTUNE): Realities, Challenges and Opportunities. *OCEANS 2007*, 1–8. https://doi.org/10.1109/OCEANS.2007.4449319

Bock, Y., Melgar, D., & Crowell, B. W. (2011). Real-Time Strong-Motion Broadband Displacements from Collocated GPS and Accelerometers. *Bulletin of the Seismological Society of America*, *101*(6), 2904–2925. https://doi.org/10.1785/0120110007

Boore, D. M. (2001). Effect of baseline corrections on displacements and response spectra for several recordings of the 1999 Chi-Chi, Taiwan, earthquake. *Bulletin of the Seismological Society of America*, *91*(5), 1199–1211.

Boore, D. M., Stephens, C. D., & Joyner, W. B. (2002). Comments on Baseline Correction of Digital Strong-Motion Data: Examples from the 1999 Hector Mine, California, Earthquake. *Bulletin of the Seismological Society of America*, *92*(4), 1543–1560. https://doi.org/10.1785/0120000926

Chadwick, W., Nooner, S., Zumberge, M., Embley, R., & Fox, C. (2006). Vertical deformation monitoring at Axial Seamount since its 1998 eruption using deep-sea pressure sensors. *Journal of Volcanology and Geothermal Research*, *150*, 313–327.

Chernick, M. (2007). *Bootstrap Methods: A Guide for Practitioners and Researchers*. Wiley.

Clawpack Development Team. (2022). *Clawpack software*. https://doi.org/10.5281/zenodo.7026045

GEBCO. (2023). *The General Bathymetric Chart of the Oceans* [dataset]. https://doi.org/10.5285/f98b053b-0cbc-6c23-e053-6c86abc0af7b

Geng, J., Bock, Y., Melgar, D., Crowell, B. W., & Haase, J. S. (2013). A new seismogeodetic approach applied to GPS and accelerometer observations of the 2012 Brawley seismic swarm: Implications for earthquake early warning. *Geochemistry, Geophysics, Geosystems*, *14*(7), 2124–2142. https://doi.org/10.1002/ggge.20144

Hilmo, R., & Wilcock, W. S. D. (2020). Physical Sources of High-Frequency Seismic Noise on Cascadia Initiative Ocean Bottom Seismometers. *Geochemistry, Geophysics, Geosystems*, *21*(10), e2020GC009085. https://doi.org/10.1029/2020GC009085

Hino, R., Kubota, T., Chikasada, N. Y., Ohta, Y., & Otsuka, H. (2022). Assessment of S-net seafloor pressure data quality in view of seafloor geodesy. *Progress in Earth and Planetary Science*, *9*(1), 73. https://doi.org/10.1186/s40645-022-00526-y

Iwan, W. D., Moser, M. A., & Peng, C.-Y. (1985). Some observations on strong-motion earthquake measurement using a digital accelerograph. *Bulletin of the Seismological Society of America*, *75*(5), 1225–1246.

Kalman, R. E. (1960). A New Approach to Linear Filtering and Prediction Problems. *Journal of Basic Engineering*, *82*(1), 35–45. https://doi.org/10.1115/1.3662552

Kamei, R., Pratt, R. G., & Tsuji, T. (2012). Waveform tomography imaging of a megasplay fault system in the seismogenic Nankai subduction zone. *Earth and Planetary Science Letters*, *317–318*, 343–353. https://doi.org/10.1016/j.epsl.2011.10.042

Koketsu, K., Miyake, H., & Suzuki, H. (2012). *Japan Integrated Velocity Structure Model Version 1*. The 15th World Conference on Earthquake Engineering, Lisboa. https://www.iitk.ac.in/nicee/wcee/article/WCEE2012_1773.pdf

Kubota, T., Suzuki, W., Nakamura, T., Chikasada, N. Y., Aoi, S., Takahashi, N., & Hino, R. (2018). Tsunami source inversion using time-derivative waveform of offshore pressure records to reduce effects of non-tsunami components. *Geophysical Journal International*, *215*(2), 1200–1214. https://doi.org/10.1093/gji/ggy345

Lawson, C., & Hanson, R. (1995). *Solving least squares problems*. Society for Industrial and Applied Mathematics.

Lewis, F., Xie, L., & Popa, D. (2008). *Optimal and Robust Estimation: With an Introduction to Stochastic Control Theory* (2nd ed.). CRC Press.

Maeda, T., Takemura, S., & Furumura, T. (2017). OpenSWPC: An open-source integrated parallel simulation code for modeling seismic wave propagation in 3D heterogeneous viscoelastic media. *Earth, Planets and Space*, *69*(1), 102. https://doi.org/10.1186/s40623-017-0687-2

Mandli, K. T., Ahmadia, A. J., Berger, M., Calhoun, D., George, D. L., Hadjimichael, Y., Ketcheson, D. I., Lemoine, G. I., & LeVeque, R. J. (2016). Clawpack: Building an open source ecosystem for solving hyperbolic PDEs. *PeerJ Computer Science*, *2*, e68. https://doi.org/10.7717/peerj-cs.68

Matsumoto, K., Takanezawa, T., & Ooe, M. (2000). Ocean tide models developed by assimilating TOPEX/POSEIDON altimeter data into hydrodynamical model: A global model and a regional model around Japan. *Journal of Oceanography*, *56*(5), 567–581.

Melgar, D., Bock, Y., Sanchez, D., & Crowell, B. W. (2013). On robust and reliable automated baseline corrections for strong motion seismology. *Journal of Geophysical Research: Solid Earth*, *118*(3), 1177–1187. https://doi.org/10.1002/jgrb.50135

Mizutani, A., Yomogida, K., & Tanioka, Y. (2020). Early Tsunami Detection With Near-Fault Ocean-Bottom Pressure Gauge Records Based on the Comparison With Seismic Data. *Journal of Geophysical Research: Oceans*, *125*(9), e2020JC016275. https://doi.org/10.1029/2020JC016275

National Research Institute for Earth Science and Disaster Resilience (NIED). (2019). *NIED DONET*. https://doi.org/10.17598/nied.0008

Niu, J., & Xu, C. (2014). Real-Time Assessment of the Broadband Coseismic Deformation of the 2011 Tohoku-Oki Earthquake Using an Adaptive Kalman Filter. *Seismological Research Letters*, *85*(4), 836–843. https://doi.org/10.1785/0220130178

Saito, T. (2013). Dynamic tsunami generation due to sea-bottom deformation: Analytical representation based on linear potential theory. *Earth, Planets and Space*, *65*(12), 1411–1423.

Saito, T., & Tsushima, H. (2016). Synthesizing ocean bottom pressure records including seismic wave and tsunami contributions: Toward realistic tests of monitoring systems. *Journal of Geophysical Research: Solid Earth*, *121*(11), 8175–8195. https://doi.org/10.1002/2016JB013195

Takemura, S., Kimura, T., Saito, T., Kubo, H., & Shiomi, K. (2018). Moment tensor inversion of the 2016 southeast offshore Mie earthquake in the Tonankai region using a three-dimensional velocity structure model: Effects of the accretionary prism and subducting oceanic plate. *Earth, Planets and Space*, *70*(1), 50. https://doi.org/10.1186/s40623-018-0819-3

Trowbridge, J., Weller, R., Kelley, D., Dever, E., Plueddemann, A., Barth, J. A., & Kawka, O. (2019). The Ocean Observatories Initiative. *Frontiers in Marine Science*, *6*. https://www.frontiersin.org/articles/10.3389/fmars.2019.00074

Tu, R., Wang, R., Walter, T. R., & Diao, F. (2014). Adaptive recognition and correction of baseline shifts from collocated GPS and accelerometer using two phases Kalman filter. *Advances in Space Research*, *54*(9), 1924–1932. https://doi.org/10.1016/j.asr.2014.07.008

Wallace, L. M., Araki, E., Saffer, D., Wang, X., Roesner, A., Kopf, A., Nakanishi, A., Power, W., Kobayashi, R., & Kinoshita, C. (2016). Near-field observations of an offshore Mw 6.0 earthquake from an integrated seafloor and subseafloor monitoring network at the Nankai trough, southwest Japan. *Journal of Geophysical Research: Solid Earth*, *121*(11), 8338–8351.

Wang, R., Schurr, B., Milkereit, C., Shao, Z., & Jin, M. (2011). An Improved Automatic Scheme for Empirical Baseline Correction of Digital Strong-Motion Records. *Bulletin of the Seismological Society of America*, *101*(5), 2029–2044. https://doi.org/10.1785/0120110039

Webb, S. C. (1998). Broadband seismology and noise under the ocean. *Reviews of Geophysics*, *36*(1), 105–142. https://doi.org/10.1029/97RG02287

Wu, Y.-M., & Wu, C.-F. (2007). Approximate recovery of coseismic deformation from Taiwan strong-motion records. *Journal of Seismology*, *11*(2), 159–170.

Zang, J., Xu, C., Chen, G., Wen, Q., & Fan, S. (2019). Real-time coseismic deformations from adaptively tight integration of high-rate GNSS and strong motion records. *Geophysical Journal International*, *219*(3), 1757–1772. https://doi.org/10.1093/gji/ggz397